

# Stretching of material lines in shock-accelerated gaseous flows

S. Kumar, G. Orlicz, C. Tomkins, C. Goodenough, and K. Prestridge  
*Physics Division, Los Alamos National Laboratory, Los Alamos, New Mexico 87545*

P. Vorobieff  
*Department of Mechanical Engineering, University of New Mexico, Albuquerque, New Mexico 87131*

R. Benjamin  
*Physics Division, Los Alamos National Laboratory, Los Alamos, New Mexico 87545*

(Received 25 January 2005; accepted 8 July 2005; published online 23 August 2005)

A Mach 1.2 planar shock wave impulsively accelerates one of five different configurations of heavy-gas ( $\text{SF}_6$ ) cylinders surrounded by lighter gas (air), producing one or more pairs of interacting vortex columns. The interaction of the columns is investigated with planar laser-induced fluorescence in the plane normal to the axes of the cylinders. For the first time, we experimentally measure the early time stretching rate (in the first 220  $\mu\text{s}$  after shock interaction before the development of secondary instabilities) of material lines in *shock-accelerated gaseous flows* resulting from the Richtmyer-Meshkov instability at Reynolds number  $\sim 25\,000$  and Schmidt number  $\sim 1$ . The early time specific stretching rate exponent associated with the stretching of material lines is measured in these five configurations and compared with the numerical computations of Yang *et al.* [AIAA J. **31**, 854 (1993)] in some similar configurations and time range. The stretching rate is found to depend on the configuration and orientation of the gaseous cylinders, as these affect the refraction of the shock and thus vorticity deposition. Integral scale measurements fail to discriminate between the various configurations over the same time range, however, suggesting that integral measures are insufficient to characterize early time mixing in these flows. © 2005 American Institute of Physics. [DOI: [10.1063/1.2031347](https://doi.org/10.1063/1.2031347)]

## I. INTRODUCTION

The instability arising at the interface between two fluids of different densities due to the impulsive acceleration of the interface (e.g., by a shock wave) is known as the Richtmyer-Meshkov (RM) instability.<sup>1,2</sup> The complex vortex-driven flow resulting from this instability eventually becomes turbulent. This RM instability differs from the more familiar constant-acceleration Rayleigh-Taylor (RT) instability<sup>3-5</sup> by the impulsive nature of the energy input into the flow. The RM and RT instabilities have in common the physical mechanism responsible for the amplification of the initial interface perturbations, namely, baroclinic vorticity deposition at the interface due to the misalignment of density and pressure gradients. This mechanism of amplification of initial disturbance is common to buoyancy-driven instabilities.

Non-linearities come into play when the amplitude of distortion of the interface becomes comparable to a typical wavelength scale. Secondary baroclinic or shear-driven instabilities,<sup>6</sup> like Kelvin-Helmholtz instabilities, also start developing. This combination of non-linearities and secondary instabilities leads to wide ranges of scales in fluid motion that eventually lead to turbulence. The RM instability occurs in several problems of interest, such as inertial confinement fusion studies of deuterium-tritium targets,<sup>7-10</sup> natural phenomenon like supernova collapse,<sup>11,12</sup> pressure wave interaction with flame fronts,<sup>13</sup> and supersonic and hypersonic combustion.<sup>14-16</sup>

The dynamics of the flow driven by the RM instability is extremely complex. As a result, these flows are studied ex-

perimentally, analytically, and computationally through various simplified test problems. Most of the experiments<sup>17-21</sup> reported in this area have concentrated on the instability of initially single-scale (sinusoidal) or multimode perturbations in straight or conical geometries. The more complex configuration of a double interface, i.e., a gas curtain interacting with a shock wave, has been studied by Jacobs *et al.*,<sup>22</sup> Rightley *et al.*,<sup>23,24</sup> and Prestridge *et al.*<sup>25,26</sup> A comprehensive review of the RM instability is presented in the review articles by Brouillette,<sup>27</sup> Zabusky,<sup>28</sup> and Vorobieff and Kumar.<sup>29</sup>

A simple test problem to understand some aspects of the RM instability is the interaction of a shock wave with cylindrical interfaces (resulting from gaseous columns) between two gases having significantly different densities. The problem has been studied for the case of a single cylindrical column analytically,<sup>30,31</sup> computationally,<sup>16,32,33</sup> and experimentally.<sup>34-37</sup> When a shock wave interacts with a gaseous cylindrical column, it deposits vorticity at the interface. This vorticity induces motion that leads to a roll up of the cylindrical interface into a counter-rotating vortex pair. In the time evolution of this vortex pair, secondary instabilities develop on the outer edges (shear-driven) and in the core (baroclinic or shear-driven<sup>6</sup>). At later times, this growth of secondary instabilities may lead to the vortex cores becoming turbulent.

A major difficulty in the experimental investigation of the RM instability is the initial separation of the two gases. In the earlier versions of these experiments a fragile mem-

brane was used to separate the gases, but membrane fracture leads to undesirable secondary effects. The relatively recent versions of the experiments try to avoid the use of membranes by clever design of the experiment.<sup>38</sup> In terms of diagnostics, laser-sheet-based diagnostic techniques have proven more effective<sup>39,40</sup> than the schlieren technique, which uses line-of-sight integration, as they provide detailed two-dimensional flow field information by imaging a thin slice of the flow.

One of the main reasons for understanding the RM instability is to understand the physics of the resulting fluid mixing. Mixing is important in technological problems such as inertial confinement fusion because one would like to minimize the dilution of fuel with ablative material. As pointed out by Ottino,<sup>41</sup> fluid mixing does not enjoy the reputation of being a very scientific subject and, generally speaking, mixing problems in nature and technology are attacked on a case-by-case basis. Fluid mixing can be viewed in terms of creation of interfacial area and reduction of length scales.<sup>42,43</sup> The interfacial area is generated by the stretching and folding of a fluid interface due to the kinematics of the velocity field. This stretching leads to intensification of gradients that causes enhanced mass transfer, i.e., mixing. Experiments on two-dimensional unsteady cavity flows in liquids at Reynolds numbers of 40–100 have shown<sup>41,44,45</sup> that simple velocity fields can generate interfacial area at an exponential rate, thereby leading to efficient mixing. Experiments in liquids by Truesdell *et al.*<sup>46</sup> on mixing of two pulsating fluid streams in a Y connection at a low Reynolds number ( $<1$ ) show exponential growth of the interface length when the parameters of the problem lead to efficient mixing. Exponential area generation is also a signature of chaotic flows. Statistics of stretching and their multifractal properties have been studied numerically by Muzzio *et al.*<sup>47,48</sup> The first experimental measurements of stretching fields in liquids at Reynolds numbers of 40–150 have been made by Voth *et al.*<sup>49</sup> using a particle tracking technique. Analytical work in this area has been reported by Ottino,<sup>42</sup> Haller and Yuan,<sup>50</sup> and Haller.<sup>51,52</sup>

The present study focuses on experimentally measuring the rate of interfacial area generation in complex, quasi-two-dimensional, *shock-accelerated gaseous flows* at a Reynolds number of  $Re = \Gamma/\nu = 25\,000$ , where  $\Gamma$  is the circulation of a vortex and  $\nu$  is the mean kinematic viscosity of air and  $SF_6$ . The data used for measuring the area stretching rate are confined to the first 220  $\mu s$ , ensuring that the effects of diffusion are not important, as the diffusion length scale over this short time is smaller than the pixel size. The end of this time range is before the development of secondary instabilities, which occurs at  $\sim 450\, \mu s$ , and the flow becomes turbulent at  $\sim 550\, \mu s$ .<sup>53</sup> We define three time regimes for our flow:

- Early time. The time regime before the development of secondary instabilities.
- Intermediate time. The time regime from the development of secondary instabilities to the development of turbulence.
- Late time. The time regime of fully developed turbulence.

Our experiments are in the early time regime. Since the flow

is quasi-two-dimensional on the time scales of the present experiment, the interface length is a measure of surface area generation. We believe that these are the first of such experimental measurements in shock-accelerated gaseous flows. The results have relevance in understanding the mixing of fuel and oxidizer in supersonic combustion ramjet propulsion where one of the strategies is shock-induced mixing.<sup>16</sup> Other applications include some chemical reactions where the reaction rate is very sensitive to the interfacial area between the reactants. We compare our measurements with the numerical work of Yang *et al.*<sup>16</sup> who computed the stretching rates in some similar configurations. Yang *et al.*<sup>16</sup> used helium gaseous cylinders surrounded by air, while in the present experiments the gaseous cylinders are  $SF_6$ . Since the absolute values of the Atwood numbers of air- $SF_6$  (0.67) and air-helium (0.76) are similar, the stretching can be expected to be similar and a comparison is justified. Typically, this type of measurement is not possible in gases, i.e., with Schmidt number  $\sim 1$ ; however, we are able to obtain an estimate of the area stretching rate due to the very short time scales of the flow. In anticipation of exponential stretching of the interface, which is possible in such two-dimensional unsteady flows, Yang *et al.*<sup>16</sup> computed the specific stretching rate exponent,  $\lambda$ , for such flows from their numerical data. The specific stretching rate exponent is defined by

$$\frac{L(t)}{L(t=0)} = A \exp\left(\lambda \frac{t}{t_0}\right), \quad (1)$$

where  $L(t)$  (also denoted as  $L$ ) is the interface length at time  $t$ ,  $L(t=0)$  (also denoted as  $L_0$ ) is the interface length at time  $t=0$ , and  $A$  is a constant. Time  $t=0$  is taken to be the instant the shock first interacts with the gaseous-cylinder configuration. The time scale  $t_0 = D/2c_1$ , where  $c_1$  is the speed of sound in air and  $D$  the nozzle diameter, is used to normalize the time ( $t_0 = 4.48\, \mu s$  in the present study;  $t_0$  was also used by Yang *et al.*<sup>16</sup> for normalizing time) and  $L_0$  is used to normalize the interface length.

The time evolution of interacting vortex pairs generated by the interaction of a Mach 1.2 shock wave with five different configurations (see Fig. 2) of heavy-gas ( $SF_6$ ) columns in air is studied using planar laser-induced fluorescence (PLIF), and the resulting images are used to measure the interfacial area growth rate (i.e., the specific stretching rate exponent). The gaseous columns are created by allowing the heavy gas to fall under gravity. In the cases with more than one cylinder, the spacing between the centers of the cylinders,  $S$ , is  $S/D = 1.5$ , where  $D$  is the diameter of the cylinders at the nozzle ( $D = 3.1\, mm$ ). This spacing is motivated by the study of Tomkins *et al.*<sup>53,54</sup> on two gaseous cylinders at the same Mach number and in the same facility using a similar cylinder diameter. They found in their first study<sup>54</sup> that the morphology was sensitive near a spacing of  $S/D = 1.5$ . Their second study<sup>53</sup> reveals that the  $S/D = 1.5$  case exhibits the greatest rotation rate of the vortices. Their velocity data from particle-image velocimetry (PIV) measurements reveal that the circulation in the outermost vortices is about  $0.23\, m^2/s$ , giving  $Re = 25\,000$ . In the present study we expect the Reynolds number of the outermost vortices to be about the same,

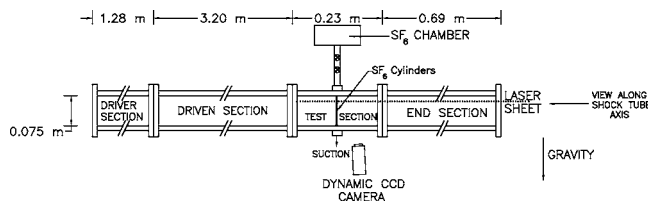


FIG. 1. Schematic of the shock tube (side view).

as the experimental conditions are nearly identical to that in the study of Tomkins *et al.*<sup>53</sup> The history of the shock refraction process in a larger gaseous cylinder is also captured with PLIF flow visualization. Shock refraction affects mixing in these flows by altering the initial vorticity distribution.

## II. EXPERIMENTAL SETUP AND DIAGNOSTIC

The experiments for this study are carried out in a horizontal shock tube of 75-mm square cross section. The flow visualization is done with planar laser-induced fluorescence (to be described in detail later in this section), and initial conditions are captured for each experiment just before the shock interacts with the gaseous cylinders. A schematic of the shock tube is shown in Fig. 1. The shock wave is generated by placing a polypropylene diaphragm at the downstream end of the driver section and pressurizing the section to  $\sim 138$  kPa (gauge). Solenoid-driven blades puncture the diaphragm, resulting in a Mach 1.2 planar shock wave propagating down the tube. Figure 1 shows the side view of the shock tube, including the camera orientation and the chamber of SF<sub>6</sub> placed above the shock tube that allows the gas to flow into the test section by gravity. Several passive flow straighteners, such as porous felt, are used to ensure laminar flow of the SF<sub>6</sub> out of the nozzle. A mild suction at the bottom of the test section removes the SF<sub>6</sub>, and a 25-mm hole downstream keeps the test section at atmospheric pressure. The vertical flow velocity ( $\sim 0.1$  m/s) of the SF<sub>6</sub> cylinders is small relative to the speed of the shock wave ( $\sim 400$  m/s) or the convection velocity of the vortical structures ( $\sim 100$  m/s), thus ensuring the quasi-two-dimensionality of the flow in the visualization plane at early times.

The center-to-center nozzle spacing between cylinders (of diameter  $D$ ) at the nozzle exit plane is denoted by  $S$ , with  $S/D=1.5$  as stated earlier. A top-view cross-section schematic of the five nozzle configurations used to form initial conditions is shown in Fig. 2. The configurations in Figs. 2(a)–2(e) will be referred to as 1C, 2C, 3C, 1C-UP, and 2C-UP, respectively. Although the nozzles have sharp edges, the gas cylinders do not. There is a reduced density gradient between the cylinders and the surrounding air caused by diffusion. Figure 3 shows the 3C geometry of SF<sub>6</sub> cylinders falling from the nozzle in a typical experimental situation. For the purpose of the visualization in Fig. 3 only, the SF<sub>6</sub> was seeded with glycol/water droplets (nominally  $0.5 \mu\text{m}$  in diameter, created with a commercial theatrical fog generator).

With the exception of Fig. 3, all of the experimental results presented in this paper were visualized using PLIF,

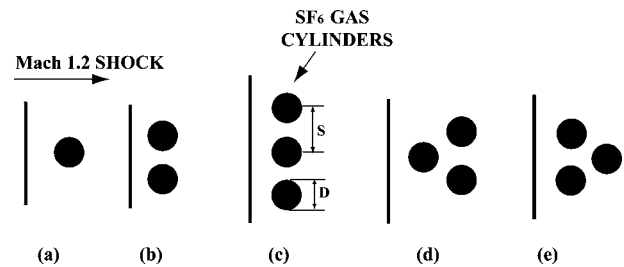


FIG. 2. Schematic of various gaseous cylinders and shock configuration,  $S/D=1.5$ : (a) 1C configuration, (b) 2C configuration, (c) 3C configuration, (d) 1C-UP configuration, and (e) 2C-UP configuration.

with acetone vapor<sup>55</sup> tracer premixed with SF<sub>6</sub> gas. The acetone tracks the SF<sub>6</sub> at a molecular level, and the acetone PLIF images have a high signal-to-noise ratio, as shown in Fig. 4. This figure illustrates not only the high signal achieved over the background, but also regions of mixed material in the vortex cores. A Nd: yttrium aluminum garnet (YAG) pulsed laser beam (Tempest-Gemini PIV from New Wave Research, Inc.) is formed into a thin ( $<1$  mm) sheet in the test section using a combination of cylindrical and spherical lenses. The power of the laser is about 20 mJ/pulse in the ultraviolet (266 nm) with 10-ns pulse lengths. Oxygen from the surrounding air that has diffused into the cylinders quenches the phosphorescence signal (relatively long time scale) from the acetone, leaving only the fluorescence signal (relatively short time scale); thus, no image blurring occurs despite a high convective velocity. The laser sheet enters the shock tube from the end section (as shown in Fig. 1) and is about 2 cm below the nozzle exit. Figure 3 also shows the location of the visualization plane. Optical access for the beam is provided by a UV-transparent window in the tube end section. The timing of the laser (and the cameras) relies on the pressure transducer located at the shock tube wall directly upstream of the test section. The laser is timed to provide one pulse immediately (about  $5 \mu\text{s}$ ) before the shock

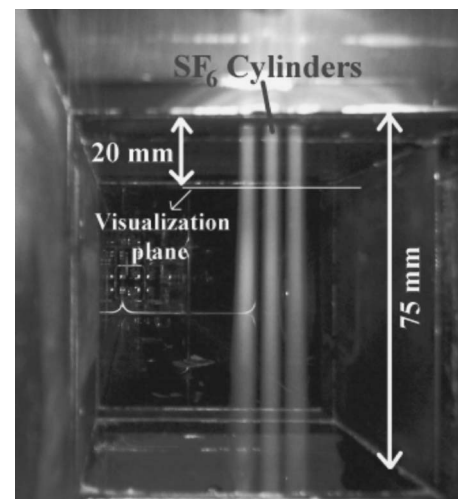


FIG. 3. Photograph of the axis view of the shock tube (looking towards the driver section) showing the three gaseous cylinders seeded with fog droplets in a typical 3C configuration.



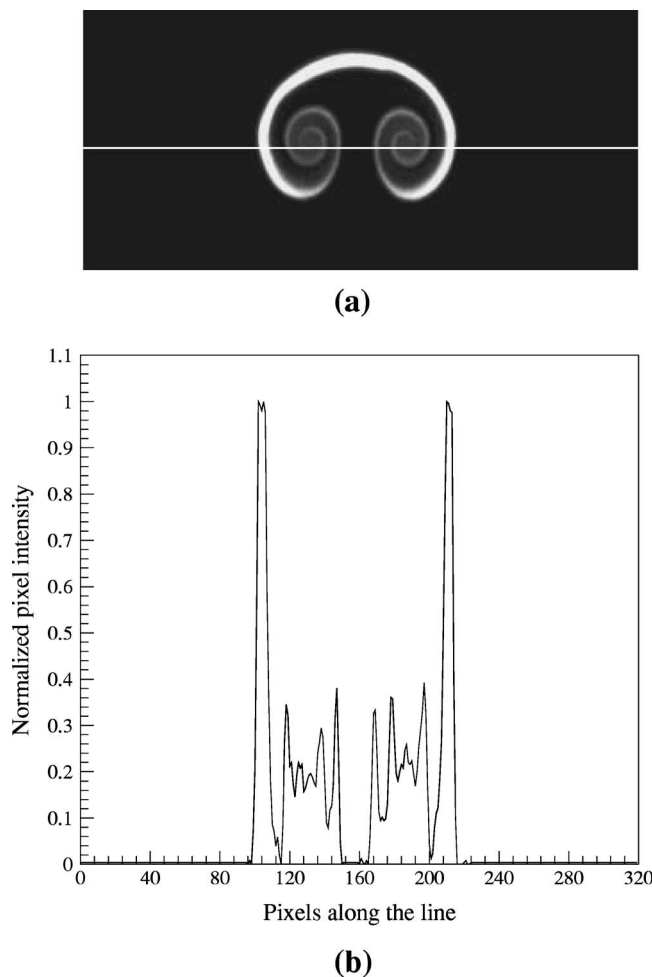


FIG. 4. Intensity profile along a line out for the IC configuration data showing the signal quality: (a) PLIF image with a line out, and (b) intensity profile along the line out in (a).

interaction with the gas cylinders, to illuminate the initial, pre-shock condition, and one pulse during the post-shock flow evolution at a specified time.

All data are acquired before the shock reflected from the end section or the rarefaction from the driver section reaches the test section. Figure 5 shows the wave diagram of the shock tube setup for current experiments. It also indicates the region in space-time where the present experiments are conducted. The initial condition and the dynamic images are captured using a 16-bit, cooled, back-illuminated Apogee  $1024 \times 1024$  charge-coupled device (CCD) camera, labeled as “Dynamic CCD camera” in Fig. 1. The camera is slightly tilted from the vertical to view the initial conditions and the dynamic image simultaneously. The resulting images are corrected for distortions resulting from the inclination of the camera. This camera captures two time-sequence images in a single frame, resulting in a double-exposed image. The dark-field of the camera and background are subtracted from the captured image, and the resulting image is then corrected for variation in the response of the CCD pixels to a uniform light source. The final processed image gives a two-dimensional estimate of the  $\text{SF}_6$  concentration with high resolution ( $78 \mu\text{m}/\text{pixel}$ ). The data are taken starting with  $t=0 \mu\text{s}$  at

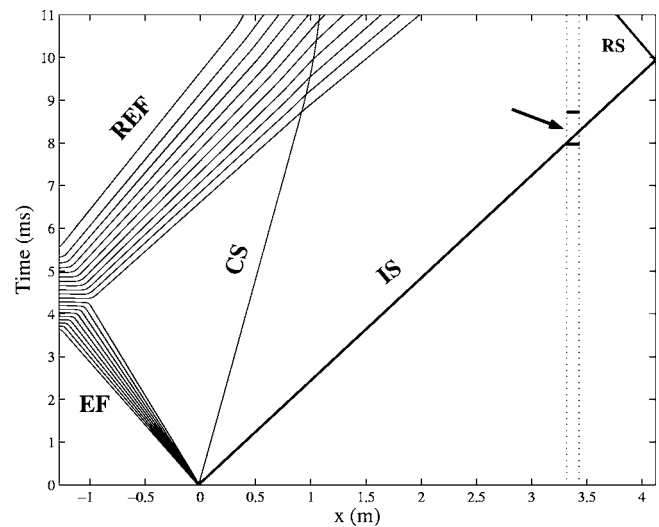


FIG. 5. Wave diagram [ $x(m)-t(ms)$  diagram] of the shock tube for present experiments.  $x=0$  is the location of the diaphragm and the dotted line represents the viewing window. IS, incident Mach 1.2 shock; RS, reflected shock; CS, contact surface; EF, expansion fan; REF, reflected expansion fan. The arrow shows the region in space-time domain where data are taken.

$15\text{-}\mu\text{s}$  intervals to about  $t=500 \mu\text{s}$  with five to six realizations at each time. A total of about 700 dynamic images were used for the present analysis.

### III. RESULTS

The flow physics of the present problem is dominated by the interaction of vortex column pairs generated by the initial baroclinic vorticity deposition. The vorticity distorts and rolls up the gaseous interface, resulting in the formation of complex flow features.

#### A. Defining a material line

The present analysis involves marking a material line in the initial condition and then tracking its development as it is stretched by the resulting complex flow. The processed PLIF images have high spatial resolution ( $78 \mu\text{m}/\text{pixel}$ ) and the time over which we track the material line growth ( $\sim$ first  $220 \mu\text{s}$ ) is small enough so that diffusion may be neglected. Moreover, if the flow is assumed to be incompressible and quasi-two-dimensional, it is correct to assume that the contour identified by a particular threshold value encloses the same material as it convects downstream and distorts due to the flow dynamics. So, the aim is to track the boundary of the structure in the ensuing motion. The boundary of the flow structures is defined by first thresholding the image and then computing the gradients of the thresholded image to define the edges. The pixels on the boundary then correspond to a set of marked fluid elements of the same concentration, since the concentration is proportional to the pixel value.

An important check to ensure that the contours of the dynamic images enclose the same material is provided by estimating the area inside the contour: it should remain constant, since the ensuing motion is incompressible<sup>35</sup> (after  $\sim 50 \mu\text{s}$  when the effect of wave reverberations inside the

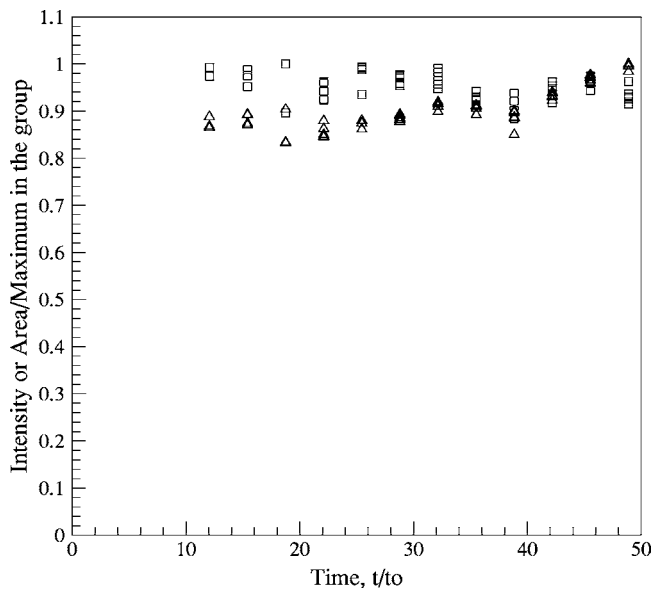


FIG. 6. Variation of area inside the contour and laser-pulse intensity with time for the 1C-UP configuration: ( $\triangle$ ) area and ( $\square$ ) intensity. Variation (one standard deviation of scatter) is 4%–5% of the mean for area and 2%–3% for intensity.

gaseous inhomogeneity has died down) and approximately two dimensional over the times considered. Figure 6 (triangle symbols) shows the area inside the contours from  $t/t_0=10$  to  $t/t_0=50$ , with  $t_0=4.48 \mu\text{s}$ , for every image measured in the 1C-UP configuration [Fig. 2(d)]. The area has been normalized by the maximum in the group. The standard deviation of the data is 4.4% of the mean value. The effect of image threshold on the area plot in Fig. 6 is negligible. By varying the threshold 20% in either direction, the standard deviation of the data changed by less than 4%. For each data set, the final threshold was chosen by minimizing this variation in area. The laser-pulse power should remain approximately the same in all the dynamic shots, so that the boundary defined by a particular threshold value is indeed the same boundary in all the dynamic images. To check this, the maximum intensity in all the dynamic images for the 1C-UP configuration is plotted with time and is shown in Fig. 6 (square symbols). The standard deviation of this maximum intensity is about 2%–3% of the mean, implying that the laser power is indeed approximately constant.

## B. Specific stretching rate exponent determination

Figure 7(a) (top row) shows the PLIF images of the initial condition and the resulting dynamic images for a single cylinder (1C) configuration at  $t=0$ , 129, 219, and 339  $\mu\text{s}$ . The bottom row in this figure shows a material line being stretched and folded. The primary roll up of the material in Fig. 7(a) (top row) is due to baroclinically deposited vorticity, and two vortices of opposite sign are formed as a result. The structure is moving at about 100 m/s. At  $t/t_0=48.9$ , the material is starting to roll up inside the vortex cores. This is also the end of the time range used for computation of the

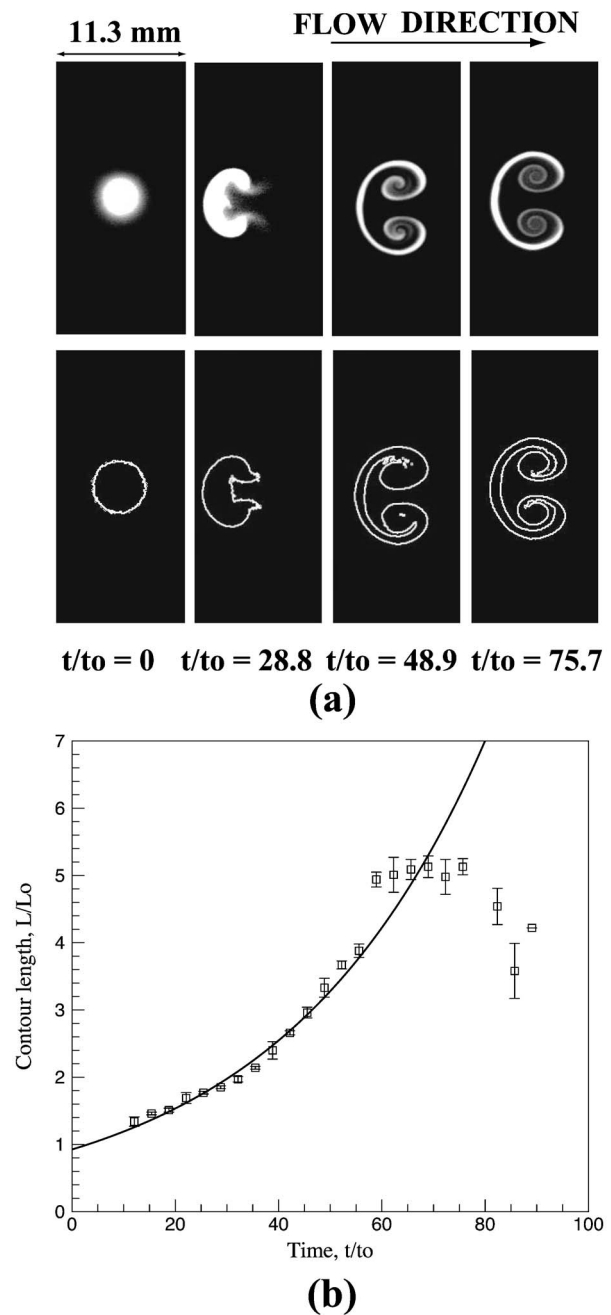


FIG. 7. Single-cylinder evolution and contour growth (1C configuration). (a) Evolution of 1C configuration at four times: top row, PLIF images at  $t/t_0=0$ ,  $t/t_0=28.8$ ,  $t/t_0=48.9$ , and  $t/t_0=75.7$ ; bottom row, corresponding contours. (b) Contour length for 1C configuration as a function of time. Solid line, exponential fit from  $t/t_0=10$  to  $t/t_0=50$ . Parameters for Eq. (1):  $A=0.926$  and  $\lambda=0.025$ .

specific stretching rate exponent because once this roll up occurs, the material lines can no longer be faithfully tracked in the cores due to the merging of the folded material which leads to the loss of monotonic increase in the material line length. This lack of resolution in tracking of the material lines starts to occur in the time range  $t/t_0=60$ –75. Consequently, for all exponents computed in this paper, the time range used to fit the data is  $t/t_0=10$  to  $t/t_0=50$ . There are about 100 data points in this time range which we believe are

sufficient to determine the curve fit accurately. This time range of the curve fit is sufficient to differentiate between a linear curve fit (corresponding to steady two-dimensional flow) and an exponential curve fit (corresponding to unsteady two-dimensional flow).

The length of the outer contour of the structures [as shown in Fig. 7(a)] is plotted in Fig. 7(b) as a function of time. The contour length is always normalized by the initial length. Each data point represents the average of five to six experimental realizations with error bars representing one standard deviation of the scatter. The exponential fit to the data gives a specific stretching rate exponent of 0.025. The data after about  $t/t_0=55$  does not strictly follow a monotonically increasing trend and is excluded from the curve fit. The specific stretching rate exponent physically tells us how fast two nearby marked fluid elements in the initial condition move apart on average (averaged over all nearby fluid element pairs in the initial condition) in the course of the complex motion induced by the shock interaction. We would like to point out that this flow is not strictly a flow generated by two-point vortices (line vortices in the present case). In the case of two-point vortex flow, the flow would be a two-dimensional steady flow (in a reference frame moving with the vortex pair) and no exponential stretching would be expected. In the present situation the initial condition of the gaseous cylinders is diffuse and therefore as the shock wave refracts inside the cylinder it deposits vorticity *field*. The unsteadiness comes from the distributed vorticity field. This vorticity field is complex and subject to a host of secondary instabilities.<sup>56</sup> The uncertainty in the measured exponent associated with the choice of times over which the fit is performed is  $\pm 0.001$ , as determined by fitting the exponential curve fits over various time ranges below  $t/t_0=50$ . A study of the effect of threshold on the specific stretching rate exponent demonstrated that even an approximate 60% change in the threshold value (corresponding to the variation in mass fraction values of  $\text{SF}_6$  from 0.04 to 0.14) changes the exponent only by  $\sim 5\%$ . The exponents are therefore robust to changes in threshold values and the ranges over which the exponential curve fit is performed.

Figure 8(a) (top row) shows the PLIF images of the initial condition and three dynamic images at identical times to that in Fig. 7(a) for the double-cylinder (2C) configuration. The second row shows the edges of the structures. Here two vortex pairs are formed as a result of shock interaction with the two gaseous cylinders. The inner two vortices are weaker than the outer vortices because the density gradients are smaller due to diffusion between the cylinders. This is evident by more roll up in the outer two vortices relative to the inner two vortices and was shown explicitly in the PIV measurements of Tomkins *et al.*<sup>53</sup> The diffused material between the two gaseous cylinders gets pushed forward [see Fig. 8(a) (top row)] and folds as the structures convect downstream. This diffused material was not captured by the Mie scattering diagnostic used by Tomkins *et al.*,<sup>53</sup> illustrating that PLIF traces diffuse species more faithfully than Mie scattering. The contour stretching for this case is plotted in Fig. 8(b). The exponential fit to the data gives the value of specific stretching exponent of 0.031. A similar study on a three-

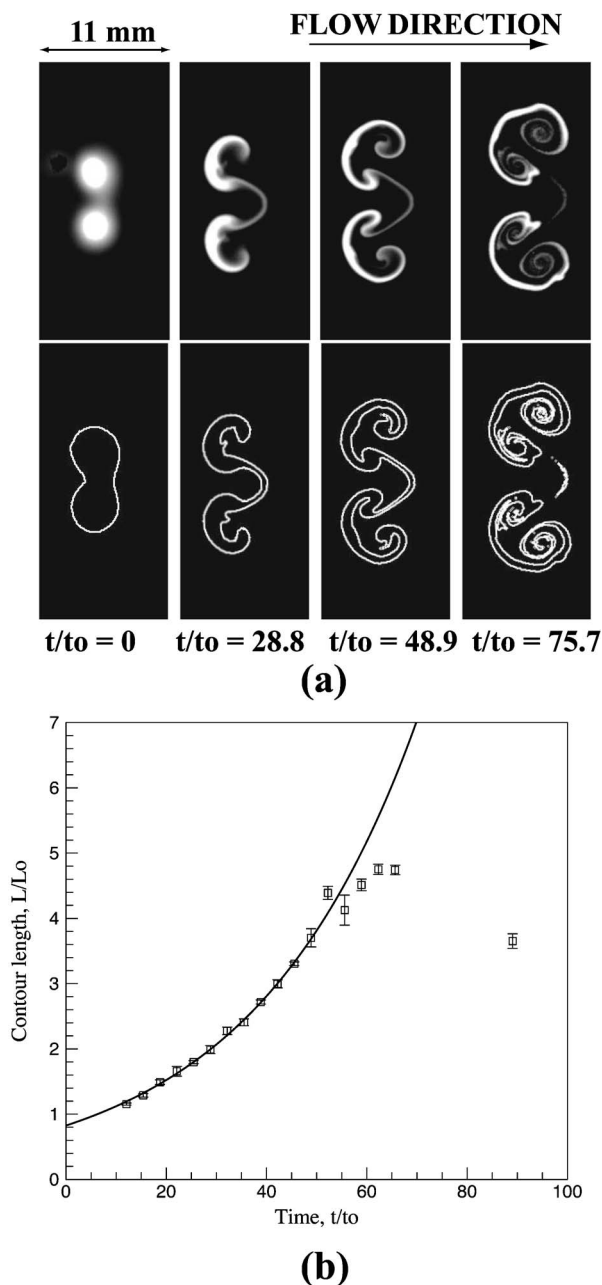


FIG. 8. Double-cylinder evolution and contour growth (2C configuration). (a) Evolution of 2C configuration at four times: top row, PLIF images at  $t/t_0=0$ ,  $t/t_0=28.8$ ,  $t/t_0=48.9$ , and  $t/t_0=75.7$ ; bottom row, corresponding contours. (b) Contour length for 2C configuration as a function of time. Solid line, exponential fit from  $t/t_0=10$  to  $t/t_0=50$ . Parameters for Eq. (1):  $A=0.826$  and  $\lambda=0.031$ .

cylinder (3C) configuration, shown in Figs. 9(a) and 9(b), gives a specific stretching exponent of 0.029 over the same time scales. This value agrees with the  $\lambda$  for the 2C case, within error, suggesting that the addition of more cylinders (above two) in the spanwise direction does not greatly enhance the mixing of the flow.

The flow morphologies resulting from the interaction of the 1C-UP and 2C-UP equilateral triangle configurations with a shock wave (Figs. 10 and 11) show very different mixing behaviors as compared to the other geometries in this study. The times for these images [Figs. 10(a)–10(d) and

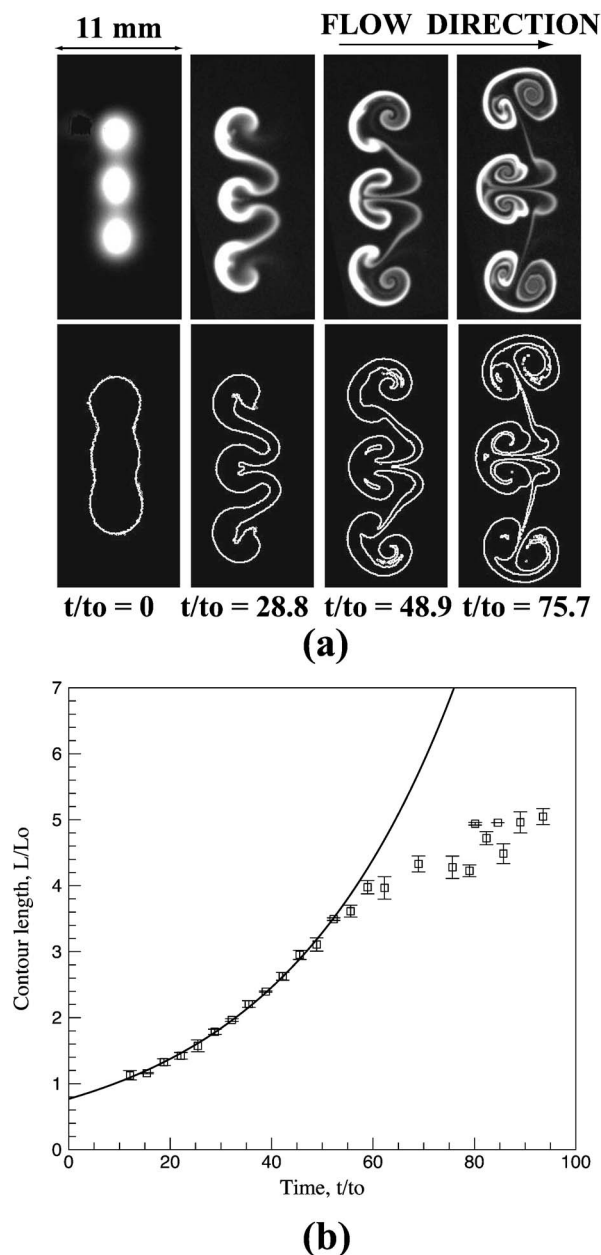


FIG. 9. Three-cylinder evolution and contour growth (3C configuration). (a) Evolution of 3C configuration at four times: top row, PLIF images at  $t/t_0 = 0$ ,  $t/t_0 = 28.8$ ,  $t/t_0 = 48.9$ , and  $t/t_0 = 75.7$ ; bottom row, corresponding contours. (b) Contour length for 3C configuration as a function of time. Solid line, exponential fit from  $t/t_0 = 10$  to  $t/t_0 = 50$ . Parameters for Eq. (1):  $A = 0.770$  and  $\lambda = 0.029$ .

11(a)–11(d) upper row] are the same as for the other configurations, i.e.,  $t = 0$ , 129, 219, and 339  $\mu\text{s}$ . The images in Figs. 10 and 11 show that the overall structure size grows faster in the spanwise direction for the 2C-UP configuration than for the 1C-UP configuration due to the motion induced by the vortices. In the 1C-UP configuration, the inner vortices of the downstream two cylinders are weaker and the inner material is pushed upstream due to the induced motion of all the other vortices. In the 2C-UP configuration, the material in the downstream cylinder is just stretched in the spanwise direction, forming a bridge between the two outer vortex pairs. This bridge stretches considerably with time, eventually

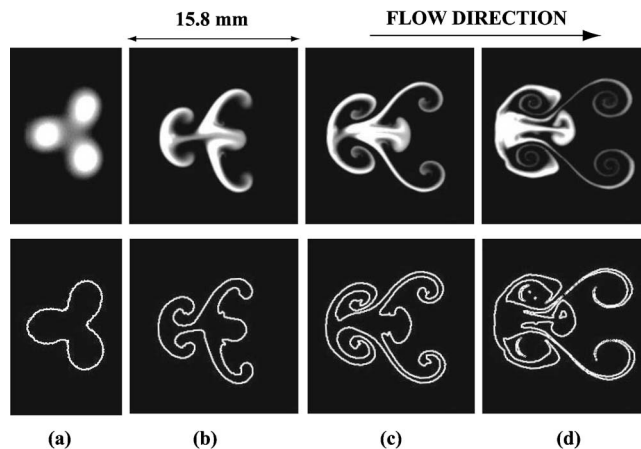


FIG. 10. Evolution of triple cylinder from 1C-UP configuration and its contour: (a)  $t/t_0 = 0$ , (b)  $t/t_0 = 28.8$ , (c)  $t/t_0 = 48.9$ , and (d)  $t/t_0 = 75.7$ .

breaking up. The contour stretching for these two configurations is plotted in Figs. 12(a) and 12(b) for the 1C-UP and 2C-UP configurations, respectively. The associated specific stretching rate exponents are calculated over the same time range as the previous geometries, and the result is  $\lambda = 0.032$  for 1C-UP and  $\lambda = 0.037$  for 2C-UP. The former is within error of the 2C and 3C geometries while the latter is noticeably higher than all the other cases.

This measurement of specific stretching rate exponents shows that in shock-induced mixing, the number, configuration, and orientation of gaseous cylinders, which in turn determines the initial vorticity distribution, matters, as far as the rate of interfacial area generation is concerned. In the five

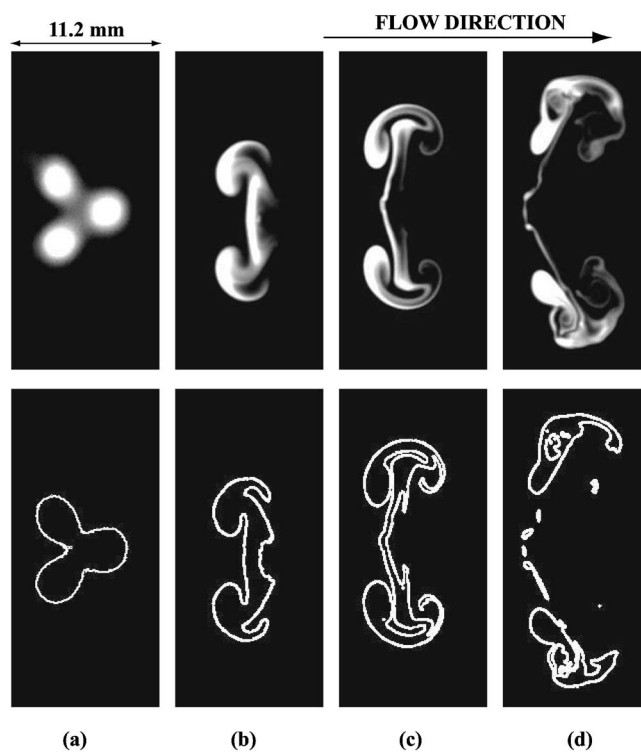


FIG. 11. Evolution of triple cylinder 2C-UP configuration and its contour: (a)  $t/t_0 = 0$ , (b)  $t/t_0 = 28.8$ , (c)  $t/t_0 = 48.9$ , and (d)  $t/t_0 = 75.7$ .



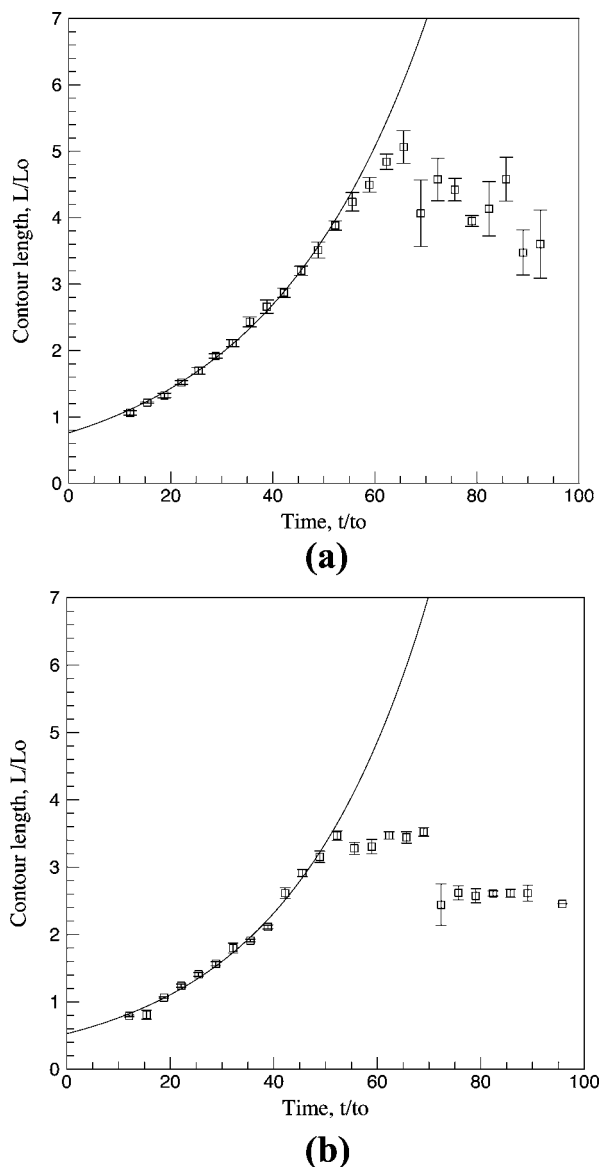


FIG. 12. Contour lengths for equilateral triangle configurations. (a) 1C-UP configuration. Solid line, exponential fit from  $t/t_0=10$  to  $t/t_0=50$ . Parameters for Eq. (1):  $A=0.760$  and  $\lambda=0.032$ . (b) 2C-UP configuration. Solid line, exponential fit from  $t/t_0=10$  to  $t/t_0=50$ . Parameters for Eq. (1):  $A=0.528$  and  $\lambda=0.037$ .

cases studied here, it appears that the 2C-UP configuration would lead to the most efficient mixing, since interfacial area is generated at the highest rate in this case. The exponential stretching seen in the present experiments is also an indication of the fact that the flow might become chaotic possibly at later times, which is possible in such two-dimensional *unsteady* flows [for stretching exponents (also called as average Lyapunov exponents in the literature) in unsteady cavity flows of liquids at Reynolds numbers  $\sim 40$ – $100$ , see Sec. 4.1 of Leong and Ottino<sup>44</sup>]. In the present experiment with gaseous shock-accelerated flows, where Reynolds numbers are  $\sim 25\,000$ , flows indeed become chaotic as they become turbulent at later times.

### C. Comparison with past numerical work and integral width measurements

The present experimental determination of specific stretching rate exponents is compared with the work of Yang *et al.*<sup>16</sup> who did a numerical study to compute these exponents for 48 different configurations. Two configurations that were common to the present study are the 1C and 1C-UP configurations. The computations of Yang *et al.*<sup>16</sup> gave specific stretching rate exponent values of 0.024 and 0.025 for the 1C and 1C-UP configurations, respectively. The experimental value of 0.025 for the 1C configuration agrees extremely well (within the experimental error bars of  $\pm 0.001$ ) with the numerics, but the agreement with the 1C-UP configuration, where the present experiments give a value of 0.032, is not very good. The specific stretching rate exponents obtained from experiments and numerics are summarized in Table I. The calculations by Yang *et al.*<sup>16</sup> used idealized initial conditions with uniform diffusion. This approximation is good for the single-cylinder geometry, where there are no surrounding structures. Both experiment and simulation of the single-cylinder geometry show similar late-time flow morphologies caused by the two equal-strength, counterrotating vortices. For the 1C-UP geometry, the idealized initial conditions of Yang *et al.*<sup>16</sup> result in flow morphologies with symmetric vortices of approximately equal strength (see their Fig. 9). Our experiment has more diffusion between the cylinders, however, resulting in density gradients that are steeper at the outer edges than in the middle. The resulting vorticity distribution is asymmetric, as can be inferred from the dynamic images in Fig. 10. Consequently, the difference in mixing and overall morphology is understandable, and it appears that the stretching, as measured by  $\lambda$ , is enhanced by the uneven distribution of vorticity. This enhancement is somewhat surprising, as the increased diffusion will lead to a reduction in the total deposited vorticity (absolute value) at early time.

In the study of the RM-instability induced flows, one of the traditional parameters of mixing is the integral scale growth rate. Here we compare this measure to the specific stretching rate exponent measure. In the present study, the integral width  $W$  is defined as the diagonal of the bounding box of the structure. The integral width for each configuration is normalized by the initial integral width  $W_0$ . Figure 13 shows the evolution of integral scales for each configuration from  $t/t_0=0$  to  $t/t_0=100$ . The image in the inset of Fig. 13 shows an example of a PLIF image with  $W$  marked. The error bars represent one standard deviation of the scatter in the data and each point plotted is the average of five to six experimental realizations. The dip between  $t/t_0=0$  and  $t/t_0=10$  is due to the initial shock compression effect. The data collapse until about  $t/t_0=50$ , which is the time limit for the use of data for specific stretching rate exponent computations. At later times, one can see the effect of moving one cylinder upstream or downstream of the two spanwise cylinders in the 1C-UP and 2C-UP configurations. The former grows the slowest while the latter grows the fastest for all the configurations studied. In the region where the data collapse (from  $t/t_0=0$  to  $t/t_0=50$ ), it is not possible to get information



TABLE I. Table summarizing the stretching rate exponents from the present experiments and computations of Yang *et al.* (Ref. 16).

Configuration	Specific stretching rate exponent (present experiments)	Specific stretching rate exponent [computations of Yang <i>et al.</i> (Ref. 16)]
1C	0.025	0.024
2C	0.031	N/A
3C	0.029	N/A
1C-UP	0.032	0.025
2C-UP	0.037	N/A

about relative fluid mixing. By contrast, the specific stretching exponents as reported in Sec. III B are able to discriminate between the various configurations, suggesting that the integral measurement is not capturing all of the subtleties of mixing in the flow.

Some of the mixing trends observed in the current experiments can be better understood by looking at the effects of shock refraction on the flow. To this end, we visualized the passage of a shock wave through a typical cylindrical density interface using PLIF. For visualization purposes, a nozzle with a larger-diameter hole (8 mm) was used to create a single heavy-gas cylinder. Figure 14 shows PLIF visualization of the passage of a Mach 1.2 shock wave through the gas cylinder. The shock front is made visible by the compression of the gas behind it. In Fig. 14(a) one can see the trace of the shock wave front just touching the upstream edge of the cylinder. This corresponds to time  $t=0 \mu\text{s}$ . Figure 14(h) shows the shock wave at about  $t=30 \mu\text{s}$  where it can be seen to be focusing on the downstream side of the cylinder. This focusing produces large pressures that eventually lead to a cusp-like protrusion, as is evident in Fig. 15 ( $t/t_0=28.8$ ). This image is the same image shown in Fig. 7(a) (top row) at  $t/t_0=28.8$ , but here different contrast levels are used to bring out the feature produced by shock focusing. This cusp-like

feature disappears in later-time images because it merges with the material behind it due to the induced motion of the outer vortices. The evidence for a cusp-like feature was also faintly seen in the PLIF images in Figs. 4(d) and 4(e) of Jacobs.<sup>36</sup> Figure 14 [compare frames (a) and (h)] also clearly shows that the shock temporarily compresses the structures; this compression is manifested as a reduction in the integral widths (see Fig. 13) in the time range from  $t/t_0=0$  to  $t/t_0=10$ .

While shock refraction produces this minor cusp feature, it also has a more important effect on mixing, as manifested in the late-time mixing widths plotted in Fig. 13. In this figure, we see that at late times the 2C-UP configuration has the greatest integral width, while the 1C-UP configuration has the smallest. The discrepancy between the integral widths of these two geometries can be explained by shock-refraction effects. In the 2C-UP geometry, the two upstream cylinders are struck by the normal shock, but the one downstream cylinder is struck by a highly refracted shock, apparently resulting in less vorticity deposition on the later cylinder. The effect is more pronounced in the 1C-UP geometry, where only one cylinder is struck by a normal, unrefracted shock, and the two downstream cylinders are hit by oblique shocks, apparently affecting the resulting mixing.

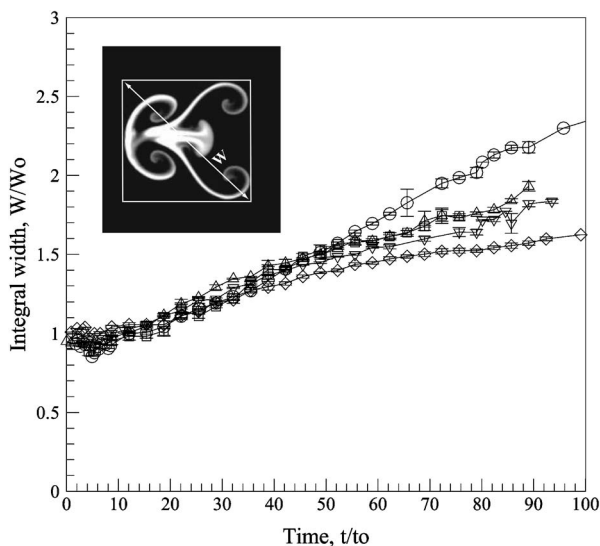


FIG. 13. Time evolution of integral scales for all configurations: ( $\square$ ) 1C configuration, ( $\triangle$ ) 2C configuration, ( $\nabla$ ) 3C configuration, ( $\diamond$ ) 1C-UP configuration, and ( $\circ$ ) 2C-UP configuration. The inset illustrates the definition of the integral width for a typical structure of 1C-UP configuration.

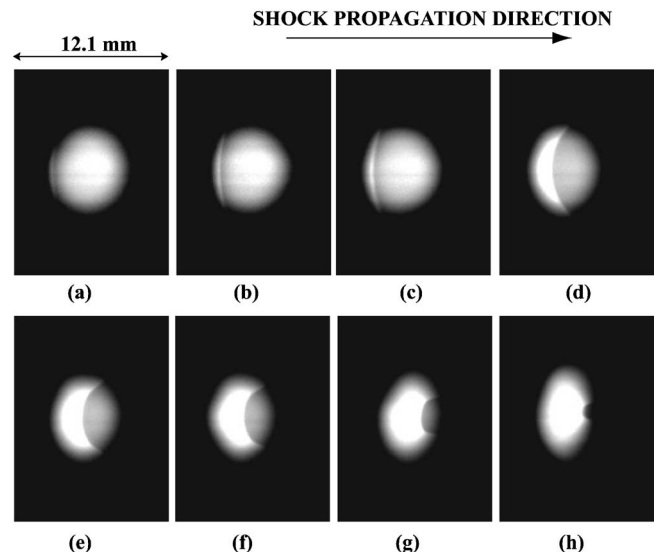


FIG. 14. Mach 1.2 shock wave propagation inside a cylindrical gaseous inhomogeneity resulting from a nozzle with an 8-mm diameter hole. Frames (a) through (h) show the time sequence at regular time intervals: (a)  $t=0 \mu\text{s}$  and (h)  $t=30 \mu\text{s}$ .

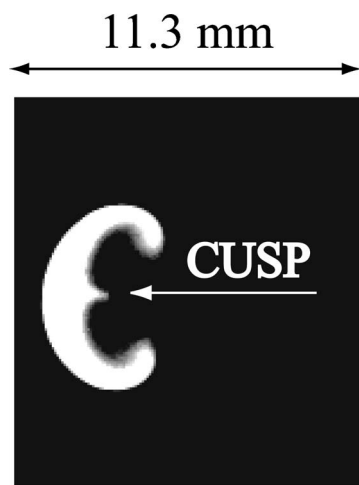


FIG. 15. Cusp-like feature in the image of Fig. 7(a) at  $t/t_0=28.8$  made visible by varying the image threshold.

#### IV. CONCLUSIONS

We studied the interaction of a Mach 1.2 shock wave with five different configurations of gaseous  $\text{SF}_6$  cylinders in air using PLIF. The early time (first 220  $\mu\text{s}$  after shock impact) specific stretching rate exponent of the stretching of material lines was measured for the first time for such shock-accelerated gaseous flows at Reynolds numbers of about 25 000. It was found that the number, configuration, and orientation of gaseous cylinders affects the shock-induced mixing in terms of the generation of interfacial area. Comparison with the past numerical work of Yang *et al.*<sup>16</sup> showed good agreement for the single-cylinder configuration. A similar comparison for the 1C-UP configuration, however, shows a significant difference in the specific stretching rate exponent, likely due to differences in the diffusion of the initial conditions. Interestingly, increased stretching is observed with reduced deposited vorticity in this case. The late-time behavior of these flows, as measured by integral width, is impacted by shock refraction when upstream interfaces perturb the shock front.

The specific stretching rate exponent appears to be a good measure of early time mixing behavior, especially since the integral mixing widths collapse at early times and are insufficient to distinguish the flows. Late-time mixing measures for gaseous flows that capture detailed, small-scale mixing differences need to be explored. The effects of Mach number, cylinder diameter, and Atwood ratio (among other parameters) on the specific stretching rate exponents also need further investigation.

#### ACKNOWLEDGMENTS

One of the authors (S.K.) would like to thank Professor Hans G. Hornung and Professor Paul E. Dimotakis of GALCIT-Caltech for useful discussions during the course of this study. We would also like to thank Mark Marr-Lyon of LANL for useful suggestions and help in experimental setup. This work was supported by Department of Energy Contract

No. W-7405-ENG-36, Task Order BG109, supporting the research at University of New Mexico.

- <sup>1</sup>R. D. Richtmyer, "Taylor instability in shock acceleration of compressible fluids," *Commun. Pure Appl. Math.* **8**, 297 (1960).
- <sup>2</sup>E. E. Meshkov, "Instability of the interface of two gases accelerated by a shock wave," *Sov. Fluid Dyn.* **4**, 101 (1969).
- <sup>3</sup>W. S. Jevons, "On the cirrus form of cloud," *Philos. Mag.* **14**, 22 (1857). Jevons was the first investigator to do controlled laboratory experiments on this instability, and these motivated Rayleigh to develop a theory.
- <sup>4</sup>L. Rayleigh, "Investigation of the character of the equilibrium of an incompressible heavy fluid of variable density," *Proc. London Math. Soc.* **II**, 200 (1883).
- <sup>5</sup>G. I. Taylor, "The instability of liquid surfaces when accelerated in a direction perpendicular to their planes-I," *Proc. R. Soc. London, Ser. A* **201**, 192 (1950).
- <sup>6</sup>P. Vorobieff, C. Tomkins, S. Kumar, C. Goodenough, N. G. Mohamed, and R. F. Benjamin, "Secondary instabilities in shock-induced transition to turbulence," *Advances in Fluid Mechanics*, edited by A. Mendes, M. Rahman, and C. A. Brebbia, Vol. 5, 139–148 (WIT-Press, 2004).
- <sup>7</sup>J. D. Lindl and W. C. Mead, "Two dimensional simulation of fluid instability in laser fusion pellets," *Phys. Rev. Lett.* **34**, 1273 (1975).
- <sup>8</sup>Yu. F. Afanas'ev, N. G. Bosov, E. G. Gamalii, O. N. Krokhin, and V. B. Rozanov, "Symmetry and stability of laser-driven compression of thermonuclear targets," *JETP Lett.* **23**, 566 (1976).
- <sup>9</sup>J. D. Lindl, R. L. McCorry, and E. M. Campbell, "Progress towards inertial confinement fusion," *Phys. Today* **45**, 32 (1992).
- <sup>10</sup>J. D. Lindl, *Inertial Confinement Fusion* (AIP, New York, 1998).
- <sup>11</sup>L. Smarr, J. R. Wilson, R. T. Barton, and R. L. Bowers, "Rayleigh-Taylor overturn in supernova core collapse," *Astrophys. J.* **246**, 515 (1975).
- <sup>12</sup>W. Arnett, J. Bahcall, R. Kirshner, and S. Woosley, "Supernova 1987A," *Annu. Rev. Astron. Astrophys.* **27**, 629 (1989).
- <sup>13</sup>G. H. Markstein, "Flow disturbances induced near a slightly wavy contact surface, or flame front, traversed by a shock wave," *J. Aeronaut. Sci.* **24**, 238 (1957).
- <sup>14</sup>F. E. Marble, G. J. Hendricks, and E. E. Zukoski, "Progress towards shock enhancement of supersonic combustion process," *AIAA Paper No. 87–1880* (1987).
- <sup>15</sup>I. A. Waitz, F. E. Marble, and E. E. Zukoski, "An investigation of a contoured wall injector for hypervelocity mixing augmentation," *AIAA Paper No. 91–2265* (1991).
- <sup>16</sup>J. Yang, T. Kubota, and E. E. Zukoski, "Applications of shock-induced mixing to supersonic combustion," *AIAA J.* **31**, 854 (1993).
- <sup>17</sup>M. Vetter and B. Sturtevant, "Experiments on the Richtmyer-Meshkov instability of an Air/SF<sub>6</sub> interface," *Shock Waves* **4**, 247 (1995).
- <sup>18</sup>J. Jacobs and J. Sheeley, "Experimental study of incompressible Richtmyer-Meshkov instability," *Phys. Fluids* **8**, 405 (1996).
- <sup>19</sup>O. Sadot, L. Erez, D. Alon, L. Oron, L. A. Levin, G. Erez, G. Ben-Dor, and D. Shvarts, "Study of nonlinear evolution of single-mode and two bubble interaction under Richtmyer-Meshkov instability," *Phys. Rev. Lett.* **80**, 1654 (1998).
- <sup>20</sup>J. K. Prasad, A. Rasheed, S. Kumar, and B. Sturtevant, "The late time development of Richtmyer-Meshkov instability," *Phys. Fluids* **12**, 2108 (2000).
- <sup>21</sup>S. Kumar, H. G. Hornung, and B. Sturtevant, "Growth of shocked gaseous interfaces in a conical geometry," *Phys. Fluids* **15**, 3194 (2003).
- <sup>22</sup>J. W. Jacobs, D. G. Jenkins, and R. F. Benjamin, "Nonlinear growth of the shock accelerated instability of a thin fluid layer," *J. Fluid Mech.* **295**, 23 (1995).
- <sup>23</sup>P. Rightley, P. Vorobieff, and R. F. Benjamin, "Evolution of a shock accelerated thin fluid layer," *Phys. Fluids* **9**, 1770 (1997).
- <sup>24</sup>P. Rightley, P. Vorobieff, R. Martin, and R. F. Benjamin, "Experimental observations of the mixing transition in a shock accelerated gas curtain," *Phys. Fluids* **11**, 186 (1999).
- <sup>25</sup>K. Prestridge, P. Rightley, P. Vorobieff, R. Benjamin, and N. Kurnit, "Simultaneous density-field visualization and PIV of a shock-accelerated gas curtain," *Exp. Fluids* **29**, 339 (2000).
- <sup>26</sup>K. Prestridge, P. Vorobieff, P. Rightley, and R. Benjamin, "Validation of an instability growth model using particle image velocimetry measurements," *Phys. Rev. Lett.* **84**, 4353 (2000).
- <sup>27</sup>M. Brouillette, "The Richtmyer-Meshkov instability," *Annu. Rev. Fluid Mech.* **34**, 445 (2002).
- <sup>28</sup>N. Zabusky, "Vortex paradigm for accelerated inhomogeneous flows for

- the Rayleigh-Taylor and Richtmyer-Meshkov environments," *Annu. Rev. Fluid Mech.* **31**, 495 (1999).
- <sup>29</sup>P. Vorobieff and S. Kumar, "Experimental studies of Richtmyer-Meshkov instability," *Recent Research Developments in Fluid Dynamics*, Vol. 5, 33–55 (Transworld Research Network, Trivandrum, India, 2004).
- <sup>30</sup>R. Samtaney and N. Zabusky, "Circulation deposition on shock-accelerated planar and curved density-stratified interfaces: Models and scaling laws," *J. Fluid Mech.* **269**, 45 (1994).
- <sup>31</sup>J. M. Picone and J. P. Boris, "Vorticity generation by shock propagation through bubbles in a gas," *J. Fluid Mech.* **189**, 23 (1988).
- <sup>32</sup>J. J. Quirk and S. Karni, "On the dynamics of shock-bubble interaction," *J. Fluid Mech.* **318**, 129 (1996).
- <sup>33</sup>C. Zoldi, "A numerical and experimental study of a shock-accelerated heavy gas cylinder," Ph.D. thesis, State University of New York at Stony Brook, 2002.
- <sup>34</sup>J. F. Haas and B. Sturtevant, "Interaction of weak shock waves with cylindrical and spherical gas inhomogeneities," *J. Fluid Mech.* **181**, 41 (1987).
- <sup>35</sup>J. W. Jacobs, "Shock-induced mixing of a light-gas cylinder," *J. Fluid Mech.* **234**, 629 (1992).
- <sup>36</sup>J. W. Jacobs, "The dynamics of shock-accelerated light and heavy gas cylinders," *Phys. Fluids A* **5**, 2239 (1993).
- <sup>37</sup>K. Prestidge, C. Zoldi, P. Vorobieff, P. Rightley, and R. Benjamin, Los Alamos Technical Report No. LA-UR-00-3973, 2000.
- <sup>38</sup>M. Jones and J. Jacobs, "A membraneless experiment for the study of Richtmyer-Meshkov instability of a shock accelerated gas interface," *Phys. Fluids* **9**, 3078 (1997).
- <sup>39</sup>J. Jacobs, D. Klein, D. Jenkins, and R. Benjamin, "Instability growth patterns of a shock-accelerated thin fluid layer," *Phys. Rev. Lett.* **70**, 583 (1993).
- <sup>40</sup>J. Budzinski, R. F. Benjamin, and J. W. Jacobs, "Influence of initial conditions on the flow patterns of a shock-accelerated thin fluid layer," *Phys. Fluids* **6**, 3510 (1994).
- <sup>41</sup>J. M. Ottino, *The Kinematics of Mixing: Stretching, Chaos, and Transport* (Cambridge University Press, Cambridge, 1989). Chap. 1, Sec. 1.1, line 1.
- <sup>42</sup>J. M. Ottino, "Description of mixing with diffusion and reaction in terms of the concept of material surfaces," *J. Fluid Mech.* **114**, 83 (1982).
- <sup>43</sup>J. M. Ottino, C. W. Leong, H. Rising, and P. D. Swanson, "Morphological structures produced by mixing in chaotic flows," *Nature (London)* **333**, 419 (1988).
- <sup>44</sup>C. W. Leong and J. M. Ottino, "Experiments on mixing due to chaotic advection in a cavity," *J. Fluid Mech.* **209**, 463 (1989).
- <sup>45</sup>J. M. Ottino, "The mixing of fluids," *Sci. Am.* **260**, 56 (1989).
- <sup>46</sup>R. A. Truesdell, P. V. Vorobieff, L. A. Sklar, and A. A. Mammoli, "Mixing of a continuous flow of two fluids due to unsteady flow," *Phys. Rev. E* **67**, 066304-1 (2003).
- <sup>47</sup>F. J. Muzzio, P. D. Swanson, and J. M. Ottino, "The statistics of stretching and stirring in chaotic flows," *Phys. Fluids A* **3**, 822 (1991).
- <sup>48</sup>F. J. Muzzio, C. Meneveau, P. D. Swanson, and J. M. Ottino, "Scaling and multifractal properties of mixing in chaotic flows," *Phys. Fluids A* **4**, 1439 (1992).
- <sup>49</sup>G. A. Voth, G. Haller, and J. P. Gollub, "Experimental measurements of stretching fields in fluid mixing," *Phys. Rev. Lett.* **88**, 254501 (2002).
- <sup>50</sup>G. Haller and G. Yuan, "Lagrangian coherent structures and mixing in two-dimensional turbulence," *Physica D* **147**, 352 (2000).
- <sup>51</sup>G. Haller, "Distinguished material surfaces and coherent structures in three-dimensional fluid flows," *Physica D* **149**, 248 (2001).
- <sup>52</sup>G. Haller, "Lagrangian coherent structures from approximate velocity data," *Phys. Fluids* **14**, 1851 (2002).
- <sup>53</sup>C. Tomkins, K. Prestidge, P. Rightley, M. Marr-Lyon, P. Vorobieff, and R. Benjamin, "Quantitative study of the interaction of two Richtmyer-Meshkov-unstable gas cylinders," *Phys. Fluids* **15**, 986 (2003).
- <sup>54</sup>C. Tomkins, K. Prestidge, P. Rightley, P. Vorobieff, and R. Benjamin, "Flow morphologies of two shock-accelerated unstable gas cylinders," *J. Vision* **5**, 273 (2002).
- <sup>55</sup>A. Lozano, B. Yip, and R. K. Hanson, "Acetone: a tracer for concentration measurements in gaseous flows by planar laser-induced fluorescence," *Exp. Fluids* **13**, 369 (1992).
- <sup>56</sup>P. V. Vorobieff, N. G. Mohamed, C. Tomkins, C. Goodenough, M. Marr-Lyon, and R. F. Benjamin, "Scaling evolution in shock-induced transition to turbulence," *Phys. Rev. E* **68**, 065301 (2003).